Interactions of shock tube exhaust flows with laminar and turbulent flames

Joel E.C. Chan[1]
UNSW Australia, Sydney, NSW 2052, Australia

Paul M. Giannuzzi[2]
New Mexico Tech, Socorro, NM 87801

Kaveh R. Kabir[3]
Macquarie University, Sydney, NSW 2109, Australia

Michael J. Hargather[4]
New Mexico Tech, Socorro, NM 87801

Graham C. Doig[5]
California Polytechnic State University, San Luis Obispo, CA, 93047

The interactions of flow features emitting from open-ended shock tubes with free-standing propane flames have been investigated using high-speed schlieren imaging and high-frequency pressure measurements, with additional data from validated numerical modeling. Both compressed air-driven interactions with non-pre-mixed laminar diffusion flames (small-scale) and explosively-driven interactions with turbulent non-pre-mixed turbulent flames (large-scale) were tested for various flame locations and shock tube stagnation pressures (and therefore Mach numbers). In the small-scale tests it was observed that the flames were not significantly influenced by the passage of either the initial shock if placed close to the tube exit, or the weaker pressure waves downstream if the flame was placed further away. Four types of interaction were classified, three of which led to permanent extinguishment of the flames. The most effective mechanism of extinguishment for a flame in-line with the exhaust was the axial exhaust jet of expanding air, which served to push the flame off the fuel source either at close range (Type I) or more slowly at a distance (Type II), after which rapid cessation of combustion occurred. With the flame positioned to one side of the path of the jet, strong loop vortices achieved a similar overall outcome of extinguishment, albeit with very different flame behavior in reaction to the strong turbulence and vorticity induced by the passing flow (Type III). In all cases bar one, the disruption to the fire triangle caused by these flow effects was sufficient to extinguish – rapidly and permanently – the flame. However, at a sufficient lateral offset of the flame from the shock tube exit, the strength of rotating flow being entrained into the diffusing vortex ring was not sufficient to remove and disperse the heat from the extinguished flame (Type IV), such that re-ignition could occur. By contrast, in the large-scale tests with a significantly different shock pressure profile and a flame approximately 1 order of magnitude greater, extinguishment in all cases for all shock strengths and locations was achieved by the shock itself (accelerating combustion) and the following "blast wind" impulsively moving the flame off the fuel source, with the vortices having negligible effect at the given testing locations (Type V).

---

[1] Research Assistant, UNSW Australia School of Mechanical and Manufacturing Engineering, Kensington.
[2] Research Engineer, Energetic Materials Research and Testing Center, 801 Leroy Pl.
[3] Research Associate, Macquarie University Department of Engineering, North Ryde.
[4] Assistant Professor, Department of Mechanical Engineering, 801 Leroy Pl., Socorro
[5] Assistant Professor, Aerospace Engineering Department, 1 Grand Ave. San Luis Obispo, AIAA Senior Member. Co-appointment: Adjunct Lecturer, UNSW Australia School of Mechanical and Manufacturing Engineering.

Nomenclature

t = *time from shock exiting tube*
$t*$ = *time from shock first interaction with flame or pertinent object (s)*
$t\char94$ = *time to flame extinguishment from t* (s)*
d = *burner external diameter (m)*
M = *Local Mach number*
p_T = *total pressure*
p = *static pressure*
p_S = *stagnation pressure*
r = *radial burner distance (m)*
T = *temperature (K)*

I. Introduction

For much of the 20th century, high explosives were routinely used to extinguish wild oil and gas well fires, reaching a peak in the treatment of wells following the Gulf War in the early 1990's [1]. Such a fire is characterized by an enormous flow rate of fuel, making extinguishment difficult using conventional methods of fire-fighting. In this case, explosives – and the flow features they generate - have proven to be efficient at extinguishing the fire and thus allowing safe human access to stop the flow of fuel. Despite the common use of the technique, very little is known about the interaction between shock waves and vortex rings with fire, including the exact mechanisms of extinguishment, which have until recently remained poorly characterized. It is a commonly held, anecdote-based belief that the explosion simply "sucks up" or burns all the oxygen in the vicinity of the fire, thus depriving the flames of their required fuel.

The present investigation is aimed at better understanding the phenomena involved. Using explosives and high-speed vortex rings to extinguish large fires is not a new idea and indeed one which has been proposed in literature for forest fires [2] and mine fires [4] in addition to wild well fires [3], but it is one which deserves more thorough investigation with modern experimental techniques and simulation which can discern, differentiate between, and time-resolve the mechanisms of extinguishment – the work described here represents the first stages in this process.

The present research effort is aimed at a better understanding of high speed flow and flame interaction in the continuation of work initiated in 2012 [5][6]. Those studies revolved around the interaction of flow from a compressed air-driven conventional open-ended shock tube with laminar diffusion and non-premixed Bunsen flames at various distances from the shock tube exhaust. Schlieren visualization was used at a frame rate of between 5000 and 7000fps, which was inadequate to properly visualize the passage of the shock wave and its effect on the flame. Extinguishment of the flame was observed in all cases, for all driver pressures and flame locations, but the effect of the shock passage through the flame, and the influence of the vortex ring, could not be clearly discerned.

Those preliminary tests followed largely the same procedure as the small-scale tests described here, however due to the insufficient time-resolution for observing the interaction phenomena and lack of a thorough parametric approach in terms of flame location and flow Mach number, the visualization setup was significantly improved to allow enhanced detail in the regions of interest, and the Mach number of the oncoming flow was determined for various driver pressures. Numerical work has accompanied these new tests.

A shock generated explosively and allowed to exhaust to atmosphere from a closed (shock) tube creates external, three-dimensionally-propagating flow features (initially a shock wave) with decaying intensity. The formation of vortex rings at the exhaust is a signature process that naturally involves entrainment of surrounding flow[20], and they evolve differently in the compressible and incompressible regimes [8][9][10][20], and are further affected by the shape of the shock tube exit [7][17]. Objects downstream of the shock tube will experience a nominally-planar shock front, then a high-speed, high-impulse flow following it ("blast wind"), and finally a vortex ring with induced and entrained rotating flows – often characterized further by an embedded shock central to the ring, with secondary and tertiary vortices produced under influence from shear layer instabilities [19].

The following sections present the visualization of supersonic flow created by a shock tube interacting with a Bunsen burner (non-premixed) flame – referred to as "small-scale" tests – as well as "large-scale" tests involving an explosively-driven shock tube (with Friedlander blast profile) and flame combination at approximately one order of magnitude greater size. The interactions were investigated for different shock wave Mach numbers, adjusting the distance between the exit of the shock tube and the flame as well as (in the small-scale tests) the input pressure of the driver section. The interaction with vortex rings created by the shock tube exhaust flow was also examined, including offsetting the flame laterally from the shock tube axes. Simple RANS CFD was used to fill in some gaps

in measurement in visualization to allow better characterization of the transient flowfield experienced by the flames in certain key tests.

II.   Methodology

Small-scale compressed air shock tube tests with non-pre-mixed Bunsen flame

The shock tube used was a basic, compressed air-driven device not capable of producing exactly the kind of temporal pressure profile associated with explosive events (i.e. a Friedlander-esque waveform). However, the flowfields obtained resulted in interactions not previously observed and documented, and the basic nature of these would be related to those obtainable with high explosives. The complex flow features emanating from the tube exit, including strongly-rotating vortices (with smaller counter-rotating vortices ahead of the main core) and a central jet of flow following the initial shock wave, were visualized with a high enough frequency (>20,000fps) to allow observation of the passage of the shockwave and the more intricate interactions which follow.

A schematic of the experimental setup for the small-scale tests is shown in fig. 1. The driving section of the UNSW Australia shock tube has a circular cross section of 70mm diameter, and is 1800mm long. The driven section of the shock tube has a rectangular cross section of 57mm wide and 44mm high, and is 2200mm long. The rectangular section exhaust gives the flow a distinctive distorted shape as corner effects are notable – this was primarily observed in the CFD depictions of the vortex loop.

A standard z-type Schlieren imaging system was used to observe all interactions between the exhausted flow and the flame. The light source was a quartz-halide light bulb, projecting onto collimating mirrors of focal length 1524mm. A simple knife-edge cutoff was used.

The Mach numbers of the shock waves produced for each driver pressure were determined from a series of calibration and repeatability tests using PCB 113B24 sensors able to provide a time history of pressure for each phase of the flow evolution at varied distances from the shock tube exit. The three input pressures in the driver section used were 40 psi, 60 psi, 75 psi, equal to 275kPa, 414kPa, and 517kPa respectively. These Mach numbers are plotted in fig. 2 and indicate the rapid changes in the flowfield close to the exhaust, trending towards decelerated standardization further downstream no matter the initial conditions, as would be expected. The Mach plot is used as a guideline rather than an indication of exact local values, as it presents the Mach number based on measured ambient conditions – however, the following central jet of supersonic flow, and the quasi-annular vortex loops formed at the edges of the tube exhaust, proved to be of considerably more interest than the shock itself. The uncertainty bars associated with fig. 2 are based on a standard deviation from repeatability from between 3 and 20 tests, the margins being never more than ±0.015.

The flame used was generated by a Bunsen burner fuelled by standard commercially-available propane. Although all the tests presented here were conducted using non-premixed flames, the interaction was investigated for premixed flames as well - no major differences in the interaction processes were observed.

A parametric matrix of test locations was established, as indicated in fig. 2. The flame was positioned either in direct line with the shock tube axis (x-axis), in which case it was exposed directly to the normal portion of the shock as well as the central expansion jet which followed it, or at a lateral offset (y-axis) such that direct interactions with the vortex ring could be observed. In the following sections, these locations are presented as multiples of the Bunsen outer diameter at a distance D and offset O, for instance x = 4.5d, y = 8.7d. A z-offset (vertical) was also tested, though not at significant-enough offsets to alter the behavior or result. The top of the burner was positioned in vertical alignment with the bottom of the shock tube for all tests presented here.

In all still frames presented in this manuscript, t*=0 is deemed to be the frame in which the shock wave first interacts with the flame, and is used as a baseline to standardize the results such that comparisons can be effectively made between cases as to the duration of interactions and the subsequent flow disruption.

It was proposed that four general primary outcomes could be achieved depending on flame location, classified into four types. A type I interaction would occur due to strong supersonic flow features - axial to the tube - interacting with the flame close to the shock tube exit; a type II interaction would be due to weak-pressure waves or subsonic axial flow at a much greater distance downstream of the tube exit; a type III interaction would result in the strong vortex loop from the tube exit interacting directly with the flame, and a type IV interaction would occur when the flame was outside the direct "line of fire" of either the vortex loop or central jet or shock wave, but affected by induced flow. Types I to III always resulted in the flame being extinguished, type IV extinguishment depended on the extent of lateral offset.

Large-scale explosive shock tube tests with non- pre-mixed propane burner flames

Larger-scale experiments were performed at the Energetic Materials Research and Testing Center (EMRTC) at New Mexico Tech in Socorro, New Mexico, USA. 21 tests were performed at a variety of burner positions as indicated in fig 3. with some limited repeatability testing due to a short testing period of availability on the range. A 0.61m diameter, 3.05m long, shock tube was used to direct an explosively driven shock wave toward the propane flame source. The steel shock tube was elevated so that the axis of the tube was 1.22m above the ground to reduce the influence of shock wave reflections (which, while present, generally did not interfere with the flame extinguishment). The end of the tube facing the flame source was open and the other end was blocked with an inertial wall which helped to direct more of the explosion energy toward the flame source. The explosive charge was a 1.42m length of 100-grain detcord, providing 30g of PETN explosive. This length of detcord was tightly wrapped around a 0.05m diameter cardboard tube. The charge was centered along the axis of the shock tube, a distance of 0.20m from the shock tube end closed with the inertial mass. The detcord was initiated with a RP-80 detonator. Initial calibration experiments showed that the compact detcord wrapping, position of the explosive charge, and the length of the shock tube were sufficient to result in a single, nearly-planar shock wave exiting the shock tube.

A commercial propane ring burner was used as the flame source in these tests. The burner had a 0.38 m outer diameter. Inside the outer shell there was a 0.30m diameter ring with 24 evenly-distributed holes where propane was ejected. There were also 3 support arms across the middle of the burner ring arranged in a "Y" pattern. These support arms had an additional 40 propane ejection holes distributed evenly across them. All of the holes on the burner were approximately 1.2mm diameter. The propane was non-premixed, requiring mixing with the ambient air to burn. A stand was built from steel to hold the burner so that the top surface of the burner was at the same height as the bottom of the shock tube, as per the small-scale tests. The stand had a flat metal plate on the front of it to prevent the incident shock wave from impacting the burner body itself and damaging it, however some undesirable additional interactions were therefore produced as a result. The stand was also used to mount pressure gages. Propane was fed to the burner from a regulator set at 69 kPa gage (10 psig). Additional tests were performed at a higher pressure (138 kPa, 20 psig) but no significant change in results (extinguishment behavior) were observed.

A retroreflective shadowgraph system [24] was used to image all of the tests performed. Shadowgraphy visualizes shock waves and turbulent eddies clearly, but is incapable of revealing the expansion behind the shock wave or any quantitative density measurements [23]. The primary choice of shadowgraphy here was to image the shock wave behavior and the location of the thermal plume from the flame. The retroreflective setup also lends itself well to large-field-of-view outdoor testing and is insensitive to direct sunlight. Details on the shadowgraph technique including a discussion of the light source and rod mirror choice can be found in literature [24]. The retroreflective screen was made of Scotchlite 7610 material mounted on a flexible backing 4.88m long by 2.44m high. The screen was positioned so that the shock tube axis was centered on the vertical height of the screen and the open end of the shock tube was at the right-most edge of the field of view. A Newport-Oriel 1000W arc lamp was used as the light source, which was focused onto a 45° rod mirror mounted in front of the camera lens. A Photron SA-X2 high-speed digital camera recorded images at 20,000 frames per second with a 1 µs exposure for all tests. The camera and light source were elevated on a table to be at the same height as the shock tube centerline. The overall setup is shown in the schematic of fig. 3 along with the burner position test matrix.

A Phantom v611 camera was synchronized with the Photron camera and recorded color high-speed images of the tests at 20,000 frames per second. This camera was used to correlate the time of flame extinguishment with the shock motion from the shadowgraph images. The Phantom camera had an exposure of 49 µs.

Three 345 kPa (50 psi) PCB 137B23 blast pressure pencil gages were used to record free-field static pressures during the tests. The pressure data was sampled at 500 kHz using a Tektronix oscilloscope. These gages were mounted on the burner stand, above the flame base, so that each had a clear line of sight to the shock tube exit and were aligned manually to be pointed at the shock tube exit and approximately perpendicular to the expected shock wave propagation. The location of the gages above the flame base resulted in the inability to measure pressure at the same time that the flame was on because the gages and/or connecting cables were in or too near the flame, resulting in destruction of the gages and cables. Separate tests were therefore performed at each location, one test with pressure gages and no flame, followed by a second test with no pressure gages and with a flame. Repeatability in flowfield and the measurement of it, as shown in fig. 4a, was found to be excellent.

Tests were performed at nine locations as shown schematically in fig. 3. Two tests were performed at each location: one with no flame to record the shock pressure and one with the flame on but no pressure gages. For both tests the shadowgraph imaging was performed which was used to validate that the shock propagation was consistent. The position measurements reported in Table 1 are the distance on axis from the shock tube exit to the center of the burner and the off-axis distance from the shock tube centerline to the center of the burner.

Small atmospheric variations were present between the tests that were performed outdoors over the two days including temperature and wind. The temperature throughout testing was recorded periodically to account for the variation in the speed of sound for all Mach number calculations. The wind varied in direction and magnitude throughout testing, but was always less than 4.5 m/s (10 mph). The shadowgraph and color images showed that the top of the flame and thermal plume were bent due to the wind at times, but the global flame attachment and response to the shock wave were unaffected and thus this is not treated as a variable in the results.

The peak pressure from all gage data is shown in fig. 3 with the expected pressure based on the local shock wave Mach number. The local shock wave Mach number can be converted to an overpressure using the simple gas dynamics relationship [22]. As can be seen, the predicted overpressure from this relationship is slightly higher than the measured gage pressures. The difference between the gage measurements and the predicted value is within the uncertainty of the Mach number measurement due to the discretized Mach number values.

The measured shock wave pressures have an uncertainty of about ±5 kPa based on the manufacturer's specifications and small variations in alignment, which is represented in the figure as the size of the pressure data symbols. The gages were aligned by eye to be approximately perpendicular with the shock wave propagation direction, and are estimated to be with 5 degrees of the intended direction. Cumulatively, these small variations in alignment are the primary cause of the spread in the data.

Table 1. Large-scale test matrix with relevant measured and derived parameters

Position	Radial Distance (m) | r/d	On-axis distance (m) | x/d	Off-axis distance (m) | y/d	Mach #	Extinguishment time, t* (ms)	~ Velocity of gas (m/s)
1	2.63 | 6.92	2.63 | 6.92	0 | 0	1.10	8.0 to 8.5	53
2	0.82 | 2.16	0.82 | 2.16	0 | 0	1.48	3.6	224
3	3.59 | 9.45	2.63 | 6.92	2.44 | 6.42			
4	1.78 | 4.68	1.73 | 4.55	0.42 | 1.11	1.18	6.5	97
5	0.92 | 2.42	0.82 | 2.16	0.42 | 1.11	1.42	3.8	199
6	0.92 | 2.42	0.32 | 0.84	0.86 | 2.26	1.42	5.0	199
7	2.01 | 5.29	1.73 | 4.55	1.03 | 2.71	1.15	10.0	78
8	1.72 | 4.53	1.38 | 3.63	1.03 | 2.71	1.19	5.1 to 6.5	97
9	7.85 | 20.66	7.81 | 20.55	0.76 | 2.00			

Numerical methodology: RANS CFD to simulate the small-scale experiments

Geometry description and meshing

Preliminary RANS CFD was used to both provide additional 3-dimensional, time-resolved information on the flow properties in and around the flame interaction space, and to serve as a foundation for later LES-based work which will look more closely at the shock/flame interactions with a more physically realistic model. Fine grid RANS is capable of reproducing open-ended shock tube flows nicely although the results can be highly-influenced by choice of turbulence model [18].

The finite-volume commercial software used to conduct all the simulations presented here was ANSYS FLUENT 14.5. Fully structured multi-grid meshes were constructed and run using the pressure-based coupled solver (comparisons with the density-based solver indicated negligible difference, with the coupled solver offering faster convergence). Second order upwinding was used in conjunction with a least-squares cell-based gradient evaluation scheme and first order implicit temporal discretization. Wall y^+ was kept close to 1 in all areas inside the shock tube to allow accurate near-wall modelling within each turbulence model tested; the 1-equation Spalart-Allmaras [11] and 2-equation k-ω SST model [12] were both used for comparisons, using Fluent's strain-vorticity corrected and compressible-corrected versions respectively [14].

Turbulence model comparisons are not presented here for reasons of brevity – the models produced near-identical (within 1%) pressure profiles at several test locations, including with time evolution. While there may have been more significant differences in the models' ability to describe the intricacies of the vortex loop in particular (visual comparisons were made using numerical schlieren in assessing capture of flow features in the shear layer and jet region), the high-level flow features were captured with satisfactory similarity between both, and therefore all runs presented here made use of the SST model which offered a slight distinction in better predicting crossing shocks in the jet and the shear layer thicknesses observed in the schlieren.

Since the shock tube had a rectangular driven section, this precluded the tube from be modelled as 2-dimensional axisymmetric. Hence, the shock tube had to be modelled in 3-dimensions but by applying symmetry conditions onto the horizontal and vertical planes passing through the centroid of the rectangle. Furthermore, the ambient air outside of the shock tube was also modelled since the flow features that exit the shock tube and propagate downstream were the main interest.

One problem with modelling such a long shock tube with the ambient air in 3-dimensions was that the mesh count would be too large for the simulations to be conducted efficiently using available resources. A work-around method (made feasible by the relatively long length to diameter ratios of the tube) was to obtain experimental static pressure readings at 0.68m upstream from the shock tube exit and use that as an inlet boundary input for the CFD model. A single-run full-length case was run for comparison and negligible difference in flow conditions immediately prior to the exit were obtained, validating this approach. The driven section was then meshed with 1mm long cells with 40 cells across the height and width of the rectangular cross section.

The fluid domain was meshed such that the region closer to the shock tube exit had finer mesh. This was because the region of interest was mainly within the 0.5m distance away from the shock tube exit. Two different mesh sizes were created for a grid convergence study. The coarser mesh had 2.85million cells whereas the finer mesh had 4.94 million cells. Refinement was made to the region near the shock tube exit so as to verify if the flow features exiting the shock tube were properly captured. Views of the domain and mesh details can be seen in fig. 5. It was found using a standard grid convergence index (GCI, following Roache [13]) that the finer mesh was required in order to provide an adequate 3% error deviation from the extrapolated true value of the result – this was deemed to be acceptable for the present purposes; the grid convergence values are presented in table 2.

Table 2. CFD grid convergence index (GCI) error for coarse vs. fine meshes

Grid	Error in Max. Exit Total Pressure	Error in Max. Exit Velocity	Error in Max. Total Pressure 0.05m from exit
Coarse (2.846 x 10^6 cells)	1.19%	6.88%	9.30%
Fine (4.941 x 10^6 cells)	0.39%	2.28%	3.09%

Boundary conditions

It was intended that the experimental static pressure be used as an input for the CFD model at 0.68m upstream from the shock tube exit. However, FLUENT requires additional information of total pressure and total temperature of the flow at that point in order to properly replicate the experimental condition. Since these data were not available from the experiment, it had to be overcome by appealing to 1-dimensional ideal shock tube theory. The experimental static pressure (of the flow behind the normal shock formed) was compared against theoretically calculated static pressure to confirm that the 1D shock tube theory was applicable to the shock tube which had differently shaped driver and driven sections. It was found that the largest discrepancy was only 4.7% deviation from theory. Hence, the 1D ideal shock tube theory was adopted in computing the total pressure, total temperature and static pressure required as an input for the CFD model. A comparison of the two means of specification, for 3 pressure measurement locations, as compared to low-pass filtered experimental data, is presented in fig.6 and indicated adequate correlation with experiments for the purposes of the present work – a more detailed analysis of discrepancies is required to better evaluate the relative over- and under-predictions.

The disadvantage of using the 1D ideal shock tube theory as a way of specifying the inlet conditions for the CFD model was that the flow properties behind the normal shock would not always remain constant. In fact, the flow properties would only remain constant as long as the "contact surface" (the air surface separating the driver and driven air) did not pass the 0.68m location where the CFD model is treating as an inlet. It was calculated that for the

worst case scenario (the highest driver pressure tested in the experiment), the "contact surface" would only arrive at the shock tube exit after 5.6ms. This was a relatively long time interval since the CFD simulations only simulated 5ms of flow time, which was more than sufficient to observe all the effects of the flow features as it exited the shock tube and interact with any downstream flame. In the experiments conducted, three different driver pressures were tested, namely 276kPa (40psi), 414kPa (60psi), and 517kPa (75psi). Non-reflecting pressure outlets were implemented for the farfield region. The inlet was specified as a pressure inlet for each of the three different driver pressures. The working fluid was air treated as an ideal gas with dynamic viscosity computed using the three coefficient method of the Sutherland Law. A Courant number of close to 1 was achieved in attaining a suitable timestep.

Validation against experiment

Due to the voluminous amount of total pressure data obtained from experiments, only selected comparisons will be shown and compared with CFD results here. It should be noted that the other total pressure data had been validated against experiments also. The characteristic length of d = 20mm was chosen as the non-dimensional length based on the Bunsen burner diameter that was used in the shock/flame extinguishing experiments. The centroid of the shock tube exit was given the non-dimensional coordinates (X,Y,Z) = (0,0,0). Fig. 6 shows the total pressure historyat locations from the shock tube exit. It should be noted that the duration of the time history shown was close to 3ms. In reality, the experimental data had a longer time history but the CFD simulation was only run for 5ms (of which 2ms was before the flow passed the point of interest), hence prohibiting any further time comparison. However, with the results that were obtained, it could be seen that the overall trend of the total pressure results was closely matched by the CFD.

It should be noted that the point of largest discrepancy in all figures was at the initial peak which indicated the shock wave passage. At this point, the CFD result was not able to predict the shock wave strength that was measured in the experiment. Nonetheless, the flow that followed behind the shock was well replicated by the CFD model as shown by the total pressure recovery after the shock passage. It could be seen that the fluctuations seen in the experimental results were not present in the CFD results because RANS turbulence modelling effectively smoothed out any small scale turbulent eddies, thereby giving a rather smooth plot.

A further comparison to experimental data is shown in fig. 7 as contours of density compared to the experimental schlieren – the second image indicates that the complexity of the shock pattern seen as the central supersonic jet evolves is not captured particularly well, perhaps as a function of mesh, turbulence model, or both. However, in the experiments, all flames were extinguished by the time this particular moment of the flowfield was established, and therefore it is not of significant concern to the present study.

III.   Results

Small-scale tests and comparative CFD

As an initial scenario, visualized in fig. 8, the flame was placed at x = 5d, y = 0d, and z = -1.75d from the center of the tube, i.e. close to the exhaust, and axial with the tube itself. This test highlights effectively the major flow features of the shock tube exhaust, as well as the effect on the flame in a type I interaction.

In frame a) the shock front initially meets the flame, and the shock tube exit is out of frame to the immediate left of the image. By frame b) the quasi-spherical shock wave has passed through the flame, with little discernible influence, but the following entrained subsonic flow is beginning to interact with the flame to impulsively move it off the fuel source. The vortex loop and central jet are in an embryonic state at the shock tube exit, and arrive at the flame location in frame c) close to 0.0005s after the initial interaction of the shock. The central jet of expanding supersonic flow pushes through the center of the decelerating, growing vortex loop (denoted (i)) and thus forms a secondary minor vortex loop due to extensive shear at the point denoted (ii). The flame front becomes compressed as it moves fully off the fuel source, but maintains a cohesive structure even as in frame d) the vortex loop significantly disrupts the flow at the Bunsen lip.

Between frames d) and e), major instabilities have manifested themselves in the flame and breakup is inevitable, and the flame has lost all connection with the fuel source. The central supersonic jet, showing signs of under-expansion in the shock structures forming, accelerates the movement of the flame downstream, and the jet and its bounding shear layers form a barrier between the residual heat and the fuel source. Combustion effectively ceases between frames e) and f). Frame h) is included, at a time 0.01195s after the initial interaction, to show that while the

exhaust flow becomes supersonic, the heat continues to have no access back to the fuel, and all original structures have fully dissipated. With the flame this close to the shock tube exit, clearly the oncoming axial component of flow dominates the extinguishment process and the flame structure is rapidly destroyed.

The flame has an effect ton the shock even as the shock has little instantaneous effect on the flame. The shock front appears thick due to the relatively low frame-rate (21,000) preferred for visualizing the vortex loop with as large a field of view as possible. The front becomes noticeably disrupted by the change in gas density, with the upper section of the quasi-spherical wave accelerated due to the high temperature in the flame region. Instabilities are introduced into the wave as a result, though they are not enough to instigate any kind of breakdown in the general wave structure.

When the flame is placed considerably further downstream on the central axis, at x = 25d (500mm), the type II interaction is more straightforward, and the events are more clearly sequential and spread out in time. In fig. 9, frames a) to c) confirm that the passage of the shock, weakened but still supersonic, through the flame has no distinguishable influence on the flame; at least not at the timescales being recorded for the present purposes. Were it possible to separate the shock from the strong momentum of the following flow, whether with an explosive event (as planned for upcoming tests) or a much more significant flame offset in the y or z directions, it would be reasonable to expect the development of Richtmyer-Meshkov instabilities not readily observable in these tests due to the shock alone.

The force of the following (subsonic) flow begins to move the flame impulsively off the fuel source in frame d). By the time the vortex ring and associated high-rotation flow arrives following frame e), the flame has already been pushed off the fuel by the remnants of the central jet, and combustion has effectively ceased by frame f). The structure of the residual heat is swiftly broken down into incoherence, indicating the strong level of turbulence in the flowfield and the loss of any distinct combustion feature.

When the flame is positioned at a lateral offset, the influence of the vortex ring and the entrainment of surrounding flow into that structure becomes the dominant force in extinguishment – that is, given that the shock has little influence and the central expansion jet no longer has a direct interaction with the flame, the sole dominant effect on the flame structure is exerted by the vortex ring.

Figure 10 presents a type III interaction where the flame is again located 25 d in the x-direction, but with a lateral offset of 5 d in the y-direction. Compared to the previous case in fig. 9, the distinctive difference in extinguishment behavior is clear – here, the shock again has negligible immediate influence, and the onset of strongly-rotating flow in the primary vortex loop introduces swirl into the flame region that results in less of an impulsive movement of the flame off the fuel in the axial direction, and more of a breakdown of the flame in-place due to the turbulent disruption to the combustion structure and its steady access to fuel. Between frames b) and d), the flame is initially perturbed, but is drawn back in the opposite direction by the natural rotation of the flow. The combustion process is sufficiently disrupted at the base that the rest of the flame momentarily lacks access to the incoming fuel, and the strong increase in turbulence breaks the flame down sufficiently that the heat rapidly dissipates.

Up until frame g), the rotation of the flow is sufficiently rapid that the flame cannot re-establish even though the heat remains in the immediate vicinity of the top of the burner, and eventually the dissipation of this heat negates any chance of re-ignition. This behavior supports the hypothesis that multiple flow phenomena from an explosive event may be able to achieve the same outcome, albeit by very different means, and that the lateral effectiveness can be controlled to an extent by the rate of spreading of the vortex loop.

Flame reignition was encountered at a relatively far-field offset location of x = 25d and y = 12d, as shown in fig. 11. Note the relatively long time scale taken for this to occur – re-ignition of the flame occurs at around 0.18s after the initial flow interaction, and establishes at the base of the flame before propagating back up into a coherent structure, in the final frame, over 0.7s after the shock has passed. Frame d) indicates that the combustion process had completely ceased, as in all the other cases. Therefore the continued presence of heat, coupled with the reduction in vorticity magnitude at this location (due to the significant lateral offset and the diffusion of the vortex loop far downstream of the shock tube exit), yielded conditions conducive to re-ignition.

This final scenario indicates that a limit to the effective range of extinguishment is present and is dependent on the expansion of the vortex loop - and therefore likely also on the geometry of the shock tube exhaust – and the pressure differential that exists when the vortex forms as well as the amount of heat initially present in the combustion region (i.e. the strength and size of the flame).

In fig. 12, the CFD contour plots of the velocity flow field exiting the shock tube for four different time frames are shown. These plots were taken in the x-y and x-z plane, to highlight the asymmetry in the flowfield caused by the rectangular cross section of the shock tube. From these frames and the animations they were taken from, it could be seen that the velocity contour provides information on the flow speed at different regions, the formation of Mach

diamonds, the location of the vortex loop, and the propagation of the shock front. The velocity information is of particular interest in the absence of experimental measurement at high resolution.

In the figures, the first black cross-hair nearest to the shock tube exit is the 0.05m (2.5D) mark whereas the second black cross-hair is the 0.2m (10D) mark. In the 0.06ms stage (not shown), the shock had just exited the shock tube. It could be observed that the shock front was almost planar for the front face. However, the sides of the shock had already diffracted off the edges of the shock tube and started forming a spherical shock front. The air velocity behind the shock front was mostly the same at this time. This meant that the shock intensity had not changed by much after exiting the shock tube for 0.06ms.

At 0.5ms (not shown), the shock front had become fully spherical and sped away from the jet stream behind it. Immediately behind the shock front, there was induced flow velocity. The velocity contour also indicated that the air exiting the shock tube had accelerated through expansion to above 400m/s. Two regions of high velocity were observed, one in between the vortex loop and the other at the shock tube exit. The former was caused by the ever reducing cross-sectional area created by the vortex loop, hence increasing the velocity there. The latter was caused by the under-expanded air expanding into ambient pressure.

At 0.8ms, the velocity contour showed that the Mach diamonds had formed behind the vortex loop. It could be seen that the central jet in between the vortex loop had further increased in its velocity. It should be noted that the ambient air speed of sound was 347m/s. Hence, the regions that were orange to red color were actually supersonic with respect to the global (not local) ambient air sound speed.

At 1.8ms, the shock wave had decayed significantly. The jet stream continued forming Mach diamonds outside the shock tube but it could be seen that the free jet boundary, as labeled in the velocity contour, was becoming smaller further away from the shock tube. The layer further out from the free jet boundary had lower velocity. This was the region of free shear flow that exhibited a high level of turbulence in the experimental schlieren images seen in Fig. 8. The free shear region eventually extended out to 70mm (3.5D) in the y-direction for the 3ms frame. The narrowing of the free-jet boundary meant that the under-expanded shock tube air was eventually reaching pressure equilibrium with the ambient air. At time frames 1.8ms and 3ms, the jet of air between the vortex loop had finally decelerated to subsonic velocity. The eventual velocity contour at 3ms showed that a 'spear-head' like flow front had formed due to the initial high jet velocity in between the vortex loop.

The initial rise in vortex loop velocity was expected since the vortex loop had to accelerate as it was generated. The drop in velocity after 0.24m suggested that the vortex loop was beginning to decay and lose its translational energy. So, it could be inferred that there was a period of stability for which the vortex loop maintained its kinetic energy through acceleration transitioning to entrainment. As mentioned, the vortex loop that formed had a distorted rectangular shape instead of a circular shape.

The corners of the vortex loop were protruding further out than the sides of the vortex loop, suggesting that the corners had higher velocity upon exiting the shock tube. These observations were consistent with those presented in literature [7]. When comparing the x-y plane with the x-z plane, the stretching of the vortex loop became more apparent as seen in fig. 12. Initially at 0.8ms, the vortex loop was in the same cross-sectional plane as can be deduced by the same distance of the zero velocity core from the shock tube exit. However, at 1.8ms the vortex core in the x-y plane was now behind the vortex core in the x-z plane.

At time 2.4ms, fig. 12 e) and f) show that the vortex core was no longer contained in the loop. This decaying of the vortex loop in the x-z plane was further seen at 3.0ms. The loss of energy in the vortex loop as evident in the vortex dissipation could have been caused by the initial instability produced by the distorted shape of vortex loop. For a circular axisymmetric shock tube, the vortex ring formed had been seen to last longer than 3ms after exiting the shock tube without decay in vortex ring velocity.

It was also observed that the vortex loop had virtually the same size (diameter) for the 3 different driver pressures when the vortex loop was at 0.16m (8D) and 0.34m (17D) away from the shock tube exit. Although the vortex loops arrived at those locations at different times for the different driver pressures, they seemed to be independent of the driver pressure, suggesting that the vortex loops will eventually attain the same size regardless of the driver pressure. The only noticeable difference between the vortex loops for different driver pressures was that the higher driver pressure generated a more stretched vortex loop.

For the investigation of the shock tube flow interaction with a flame, the flame was modelled as a simple region with appropriately high temperature. This was accomplished by patching a cylinder of 1300K with a diameter of D and height, 3.5D at a distance of 5D from the shock tube exit. Figure 13 shows an example test with fig. 14 showing the location of the "flame" in the ambient air domain at the start of the interaction (t* = 0) and beyond. It should be noted that since the flame height was 3.5D from the shock tube centroidal height, it will be reflected on the symmetry plane which was the x-z plane. As no ground reflections were observed, this was deemed to be an acceptable approximation. The driver pressure investigated was 414kPa (60psi) for flame position A.

Fig. 15 had been plotted to understand the interaction of the flow on the temperature of the "flame". At 0ms, it could be seen that the temperature of the air immediately behind the shock was higher than the ambient air. However, the vortex loop that was generated at the shock tube exit was cooler, at most 60 degrees below 300K. At 0.26ms, the shock wave had passed through the flame and there were no significant changes to the air temperature behind the shock wave. At this time the flame had shifted off its initial position a little but the high temperature core was largely maintained. The high temperature flame diameter at mid-height had decreased as a result of the flame being pushed to the sides.

Nonetheless, it was clear from frame 0.5ms and 0.82ms that the flow had a significant effect on reducing the flame temperature from 1300K to approximately 360K through the extreme forced convection and dispersal. This reduction in temperature could be attributed to the fast travelling flow which effectively dispersed out the high temperature air, as well as the low temperature vortex loop that followed behind the initial jet of air. At 1.3ms, the vortex loop was seen to be an effective mixing agent in re distributing the high temperature flame to the main jet stream as well as the ambient air. The temperature of the vortex loop was raised as a result. From 1.3ms onwards, the hot temperature air continued to hover above the initial location of the flame as they were not affected by the oncoming linear flow exiting the shock tube – this was observed in the experiment of fig. 13 too. Judging by the high remnant temperature at 1.3ms of Fig. 13, it could be concluded that the flame which did not come into direct contact with the vortex loop will not experience much drop in temperature.

Furthermore, the main mechanism which allowed the flame to cool was the vortex loop and the jet flow that was in front of the vortex. It was seen that the shock wave had minimal to no impact on flame. The shock wave was responsible for inducing a high velocity flow and higher temperature flow behind it, but the velocity of the air was not fast enough to push the flame away from its original location and disperse it prior to the arrival of the following flow features of vortex and jet. In fact, it was the jet in front of the vortex loop that had the higher velocity to displace the flame outwards and upwards (counter-clockwise rotation). The velocity behind the shock generated by the 414kPa driver pressure was only 81m/s when approaching the flame region whereas the jet in front of the vortex loop was approximately 200m/s – more than sufficient to cause extinction.

Large-scale tests

A sequence of images from the test at position 4 is shown in fig. 16. The images show the shock wave emerging from the shock tube and propagating downstream as a spherical wave. The air within the shock tube, which has been accelerated by the shock wave passing through it, exits and forms a large vortex ring. The vortex ring grows as it propagates downstream, carrying a clear embedded shock inside it. The shock wave impinges on the flame source, and pushes the flame, eventually, off of the burner. There is some limited evidence of an acceleration in combustion as the flame front compresses and instabilities are introduced – this requires further investigation. When the flame moves off of the burner it is extinguished. The flame is extinguished before the vortex ring reaches the burner location (as it is in all tests).

Variations on a theme are presented in fig.17, for positions 2 and 6. 6 was close to the shock tube exit in the axial sense but offset laterally – here the only significant rotation of the flame caused by the formation of the vortex ring was observed, as the flame was pushed off the fuel (towards the camera) but can be seen to "twist" and stretch in a rotational sense as it extinguishes. The lack of a second plane of view restricts interpretation of the physics. At position 2, close to the shock tube exit, the flame is pushed forcefully and directly off the fuel in the flow direction, but the local flow caused by the burner itself produced a counter-clockwise rotation on the flame as it extinguished. The pushing of the flame off the fuel source, accompanied by potential acceleration of turbulent combustion caused by the shock passage instigating small-scale, short-term instabilities, led to flame extinguishment in almost all cases before any influence of the vortex ring was felt.

The exception was position 9, where the flame was not extinguished. In this test, the shock (and ground reflection) passed through the flame at a much lower speed therefore the following air had less momentum. The much weaker shock did not push the flame off the burner. The upper portion of the flame was extinguished as in other tests, but the lower portion remained attached to the burner and eventually re-established the full flame in the presence on lingering heat and fuel. The flame may have remained attached at the base because it was slightly protected by the burner lip. It is possible that this case points more clearly towards potential for flame structure disruption due to Richtmyer-Meshkov-esque instabilities disrupting the flame structure and increasing the local rate of burning, whereas in all other cases the momentum of the high-speed flow moving with and behind the shock was enough to displace the flame off the burner. Any shock-induced influence to the rate of combustion was unclear in the absence of a reference wind-produced extinction event (no shock).

The lack of vortex influence is in distinct contrast to the small-scale flame experiments where vortex entrainment was enough to induce a breakdown into smaller turbulent structures followed by rapid flame extinction.

The shock wave position versus time was measured from the shadowgraph images using a MATLAB routine. The shadowgraph image pixel resolution was between 2.9 and 3.0 mm/pixel for all tests. The slight variation in pixel resolution was due to minor camera position differences in the setup between tests. The pixel resolution was measured by recording a calibration image of an object of known length before each test.

The shock wave velocity was calculated from the shock wave position data using a centered finite difference and converted to Mach number. The shock wave exits the tube at a nearly-constant Mach number of about 1.9, then decays toward Mach 1. The spread in the data represents the variability between tests and the discretization due to the finite difference calculation. The pixel resolution results in the Mach number being discretized at 0.087 increments.

The initially constant shock velocity is attributed to the shock tube producing a planar shock wave at the exit. The shock exits the tube as a one-dimensional shock wave, which becomes spherical as it propagates into the free field. The shock wave velocity begins to decrease at approximately 0.3m from the shock tube exit, which is approximately equal to the radius of the shock tube. After this point the shock wave velocity decays similar to a free-field explosion. The experimental data for the shock position, after a distance of 0.3m from the shock tube exit, was fit to the equation proposed by Dewey for the shock wave radius (R) versus time (t) for a free-air blast [22].

The shock Mach number versus distance graph was used to calculate the shock wave Mach number at each burner location. The burner locations are identified based on the distance from the center of the shock tube to the center of the burner. All burner locations experience a shock Mach number of less than 1.5, which is a relatively weak shock wave. The color high-speed videos were analyzed to estimate the amount of time between when the shock wave initially contacts the flame to when the flame is completely extinguished. A summary of the results was given back in Table 2. The results show that the flame is generally extinguished faster when the Mach number of the shock wave is higher. The flame is also extinguished faster if it is on-axis with the shock tube, flames off axis at the same radial distance generally take longer to be extinguished. The uncertainty in these measurements is estimated to be ±0.5 ms. Further investigation is needed to explore these results more.

IV. Conclusions

A study of the interaction of high speed flow features from an open-ended conventional shock tube with a non-premixed Bunsen flame was conducted, initially as a parametric study involving driver pressures and flame location. High speed schlieren visualization was used to observe the details of the interactions between shock waves, expansion jets, and vortex loops, with the flame at various axial and lateral locations. This was accompanied by simple RANS CFD to help better describe the flow features and understand their interactions with the flames. These tests and the CFD were followed by larger-scale testing using an explosively-driven shock tube and flame at approximately one order of magnitude greater than the initial tests, using a propane ring burner to create a turbulent non-pre-mixed flame.

The main findings can be summarized as follows:

In the small-scale tests, the through-passage of the shock wave did not have any notable effect on a flame in the timescales observed. It passes through a flame without causing it any significant movement, or disrupting its internal stability, prior to the arrival of more disruptive following flow features. This is independent of the velocity of the shock wave. The shock itself is slightly accelerated due to the increased temperature in the flame vicinity, and the shock front distorts as a result.

When the flame is in line with the shock tube axis for the small-scale tests, the rapidly-expanding flow following the shock wave causes extinguishment by impulsively pushing the heat (i.e. the flame itself) off the fuel source. The fire triangle is thus broken, preventing the continuation of the combustion process. This effect is observed regardless of whether the flow is supersonic (type I interaction) or high-subsonic (type II).

When the flame is offset so that it is caught in the vortex loop or the flow entrainment region close to it, the flame responds to the movement of the surrounding air and starts rotating. The rotation of the whole flame destroys the

connection between the fuel source and the flame, which thus starts extinguishment from the base. Concurrently, the highly-turbulent rotation disrupts the internal stability of the flame, leading to a breakdown in structure. According to the vortex loop's rotational velocity (depending on whether the vortex loop is created by a flow with enough velocity and where the flame is relative to the centre of the vortex), this can either have a very small impact on the flame (type IV interaction) or cause its extinguishment (type III). At a certain offset, the flow vorticity is not strong enough to remove or disrupt the heat sufficiently, and the flame can re-ignite from a state of no observable combustion.

In contrast to the small-scale experiments, explosively-driven shock waves were observed to extinguish flames by blowing the flames off of the fuel source with the velocity that the shock wave imparted to the ambient air. Experiments were performed with varied positions of the flame source relative to the explosively-driven shock tube, and in all cases the flame was primarily extinguished by the same mechanism. If the imparted air velocity is the only extinguishment mode for all of the scenarios tested, then the minimum air velocity needed to extinguish the flame is between 15-40 m/s. Both compression and stretching of the flames were observed but the role of a shock-induced increase in the rate of mixing and combustion was unclear and requires significant further investigation with more detailed measurements an instrumentation, better allowing scaling analysis and broader conclusions.

Work now turns to the use of high-resolution pressure sensing in order to obtain a "map" of the flow in space. This data will be used to confirm the extent of the vortex loop and its influence, as well as the evolution of the flowfield with time, but more importantly will be used to validate transient LES-based computational fluid dynamic simulations. The numerical approach can then be extended to scales and scenarios not possible in the laboratory.

References

[1] Husain, T. "Extinguishing of Kuwaiti oil fires—Challenges, technology, and success". Atmospheric Environment, Vol. 28, No. 13, 1994, pp. 2139-2147.

[2] Akhmetov, D.G., Lugovtsov, B.A., Maletin, V.A.: Vortex powder method for extinguishing a fire on sprouting gas-oil wells. In: V.E. Zarko, V. Weiser, N. Eisenreich, A.A.Vasiliev (eds.) Prevention of Hazardous Fires and Explosions, 1999, Springer, pp. 319–328.

[3] Akhmetov, D.G., Lugovtsov, B.A., Tarasov, V.F. "Extinguishing gas and oil well fires by means of vortex rings". Combustion Explosion and Shock Waves, Vol. 16, No. 5, 1980, pp. 490–494

[4] Xue, Y., Quio, X.H., Jin, G.J. "Research on ignition and extinguishing by explosion of high explosive". Blasting Vol. 2, 2009, pp. 26–30

[5] Doig, G., Johnson, Z., Mann, R. "Shock wave interaction with a flame". In: 18th Australasian Fluid Mechanics Conference, Launceston, 2012.

[6] Doig, G., Johnson, Z., Mann, R. "Interaction of a shock tube exhaust flow with a non-premixed flame". Journal of Visualization, Vol. 16, 2013, pp. 173–176

[7] Jiang, Z., Onodera, O., and Takayama, K., "Evolution of shock waves and the primary vortex loop discharged from a square cross-sectional tube". Shock Waves, Vol. 9, No. 1, 2000, pp. 1-10.

[8] Akhmetov, D.G. "Formation and basic parameters of vortex rings". Journal of Applied Mechanics and Technical Physics, Vol. 42, No. 5, 2001, pp. 794–805.

[9] Arakeri, J. H., Das, D., Krothapalli, A., Lourenco, L.. "Vortex ring formation at the open end of a shock tube: A particle image velocimetry study." Physics of Fluids, Vol. 16, no. 4, 2004, pp. 1008-1019.

[10]   De, S., Murugan T.. "Numerical simulation of shock tube generated vortex: effect of numerics." *International Journal of Computational Fluid Dynamics, Vol.* 25, No. 6, 2011, pp. 345-354.

[11]   Spalart, P. R., and Allmaras, S. R., "A One-Equation Turbulence Model for Aerodynamic Flows," La Recherche Aerospatiale, No. 1, 1994, pp. 5–21.

[12]   Menter, F.R., "Two-equation eddy-viscosity turbulence models for engineering applications". AIAA journal, 1994. Vol. 32, no. 8, pp. 1598-1605.

[13]   Roache, P. J. "Quantification of uncertainty in computational fluid dynamics." Annual Review of Fluid Mechanics 29, no. 1 1997, pp. 123-160.

[14]   Fluent User Guide: Release 14.5, ANSYS® Academic Research, ANSYS, Inc., Lebanon NH, 2011.

[15]   Kilchyk, V., Nalim, R., Merkle, C. "Laminar premixed flame fuel consumption rate modulation by shocks and expansion waves". Combustion and Flame, Vol. 158, no. 6, 2011, pp. 1140–1148.

[16]   Kilchyk, V., Nalim, R., Merkle, C. "Scaling interface length increase rates in Richtmyer-Meshkov instabilities". Journal of Fluids Engineering, Vol. 135, no. 3, 2013, pp.031,203.

[17]   Kashimura, H., Yasunobu, T., Nakayama, H., Setoguchi, T., Matsuo, K. "Discharge of a shock wave from an open end of a tube". Journal of Thermal Science, Vol. 9, no. 1, 2000, pp. 30–36.

[18]   Murugan, T., Sudipta De., Laxmana D., Das, D., "Numerical Simulation and PIV study of Formation and Evolution of Compressible Vortex Ring". Shock waves, Vol. 22, no. 1, 2012, pp. 69-83.

[19]   Murugan, T., Das, D. "Characteristics of counter-rotating vortex rings formed ahead of a compressible vortex ring". Exp. Fluids, Vol. 49, 2010, pp. 1247–1261.

[20]   Dabiri, J.O and Gharib, M. "Fluid entrainment by isolated vortex rings". J. Fluid Mech. Vol. 511, 2004, pp. 311–331.

[21]   Picone, J. M., Oran, E. S., Boris, J. P., Young Jr, T. R. "Theory of vorticity generation by shock wave and flame interactions" (Report No. NRL-MR-5366). Naval Research Laboratory, Washington DC (1984).

[22]   Dewey, J.M. "Explosive flows: Shock tubes and blast waves. In: Handbook of Flow Visualization", 1st edn., book chapter 29, pp. 481–497. Hemisphere Publishing Corp. (1989)

[23]   Hargather, M.J., Settles, G.S. "Optical measurement and scaling of blasts from gram-range explosive charges". Shock Waves, Vol. 17, 2007, pp. 215–223.

[24]   Hargather, M.J., Settles, G.S. "Retroreflective shadowgraph technique for large-scale visualization". Applied Optics Vol. 48, 2009, pp. 4449–4457.

Events
t = 0 shock exits tube
t* = 0 shock first interacts with flame (or position)
t^ = flame extinguished, from t* = 0

300mm collimating mirror(s)

mounting
board

NI DAQ and signal conditioner

metal halide
light

static *p*
PCB 113B24

total *p*
PCB 113B24 x 2

stagnation *p*   driver section   diaphragm   driven   PC
PCB 113B24   ø = 0.07m   section
                                                                0.044 x 0.057m

Bunsen flame

y

knife-edge and focusing lens

Photron SA5 camera
@ 20-50kHz

x

Fig. 1 Experimental apparatus for small-scale (compressed air shock tube) tests at UNSW Australia.
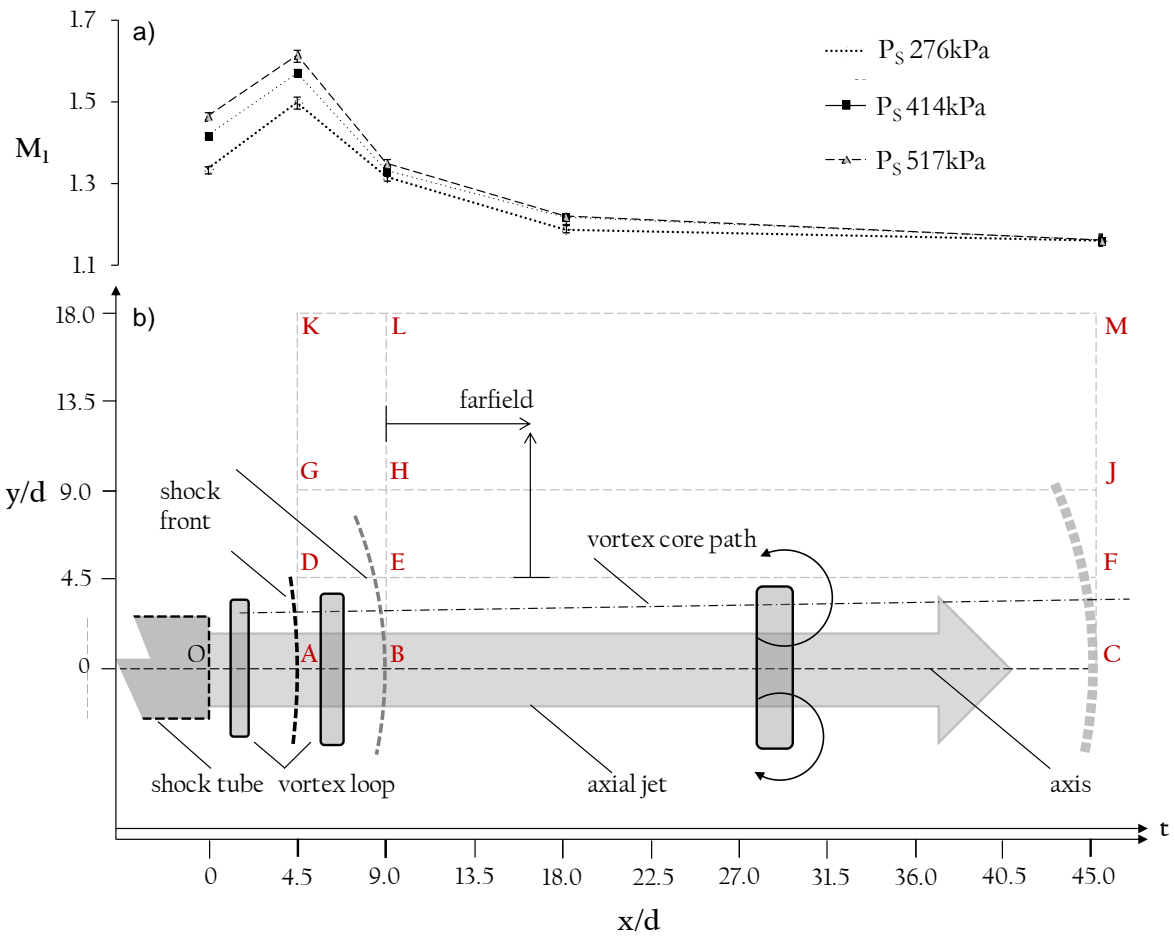
Fig. 2 Shock Mach number vs. axial distance from the shock tube exit (a), and b) schematic of matrix of test locations and representation of flow features propagating from the shock tube exit.
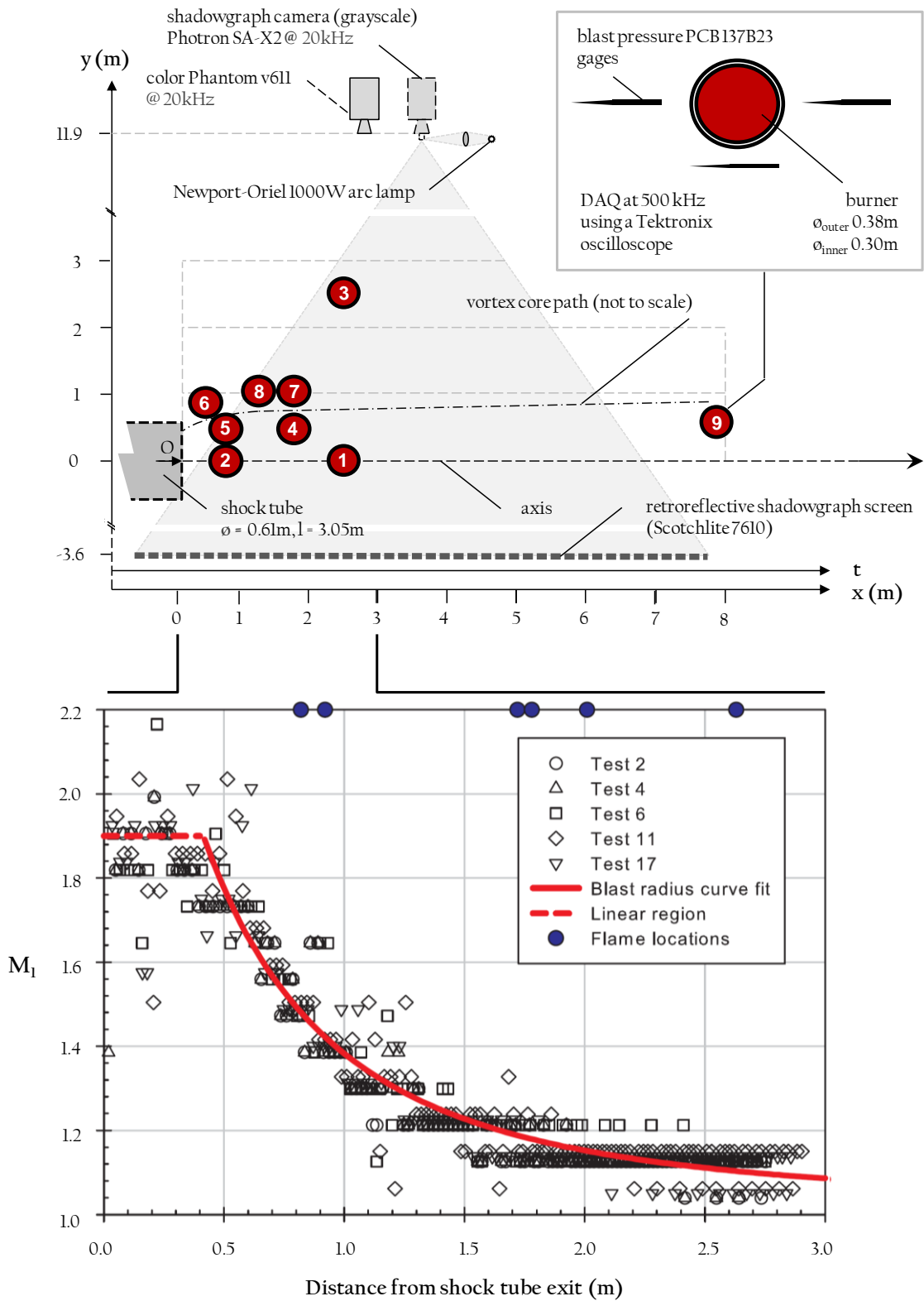
Fig. 3 Experimental apparatus and schematic of test matrix of burner locations (top) for large-scale (explosively-driven shock tube) tests at EMRTC/NMT, and (bottom) shock Mach number vs. axial distance from the shock tube exit

a)

b)
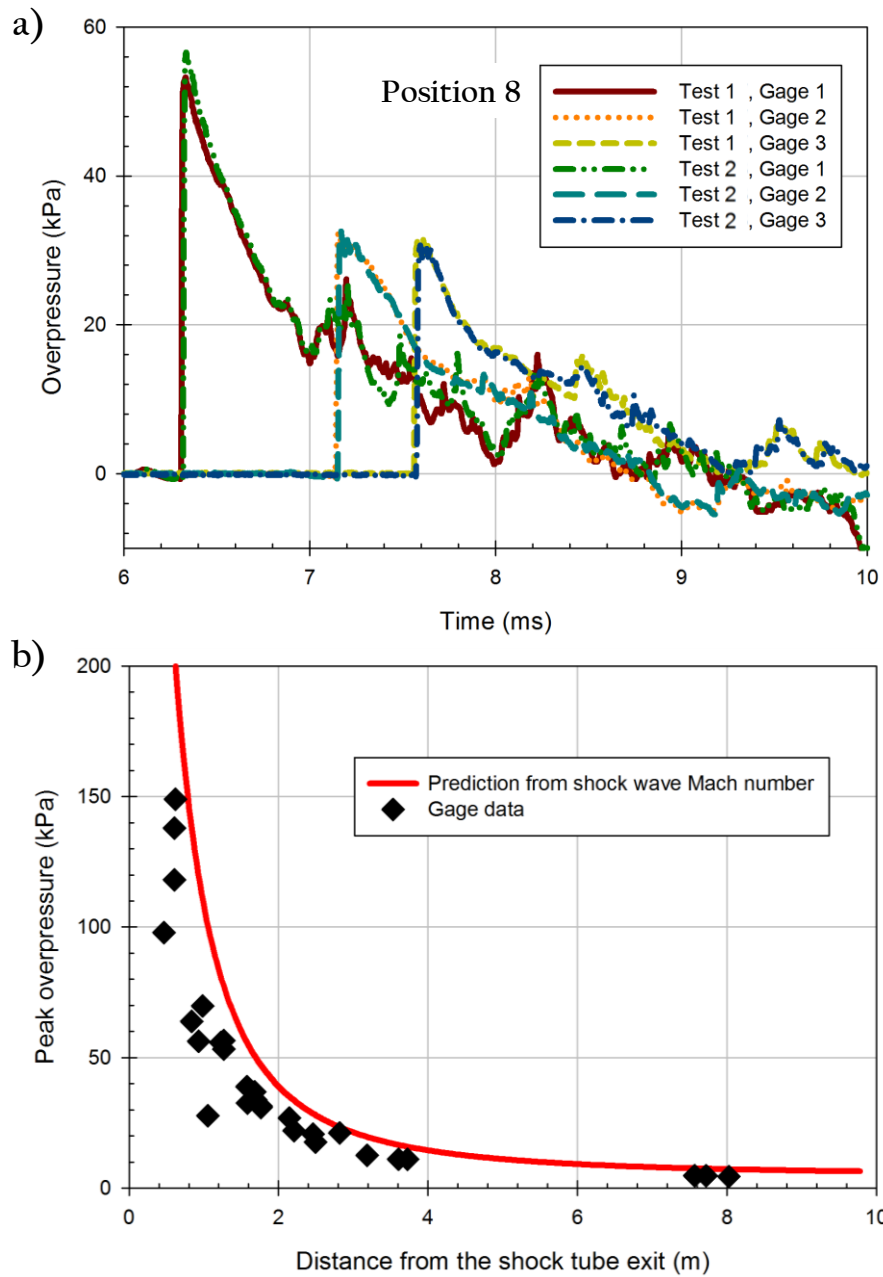
Fig. 4 a) Measured overpressure vs. time from pressure gages for repeatability at position 8, and b) measured peak overpressure vs. predicted pressure from shock Mach number vs. distance from shock tube exit.
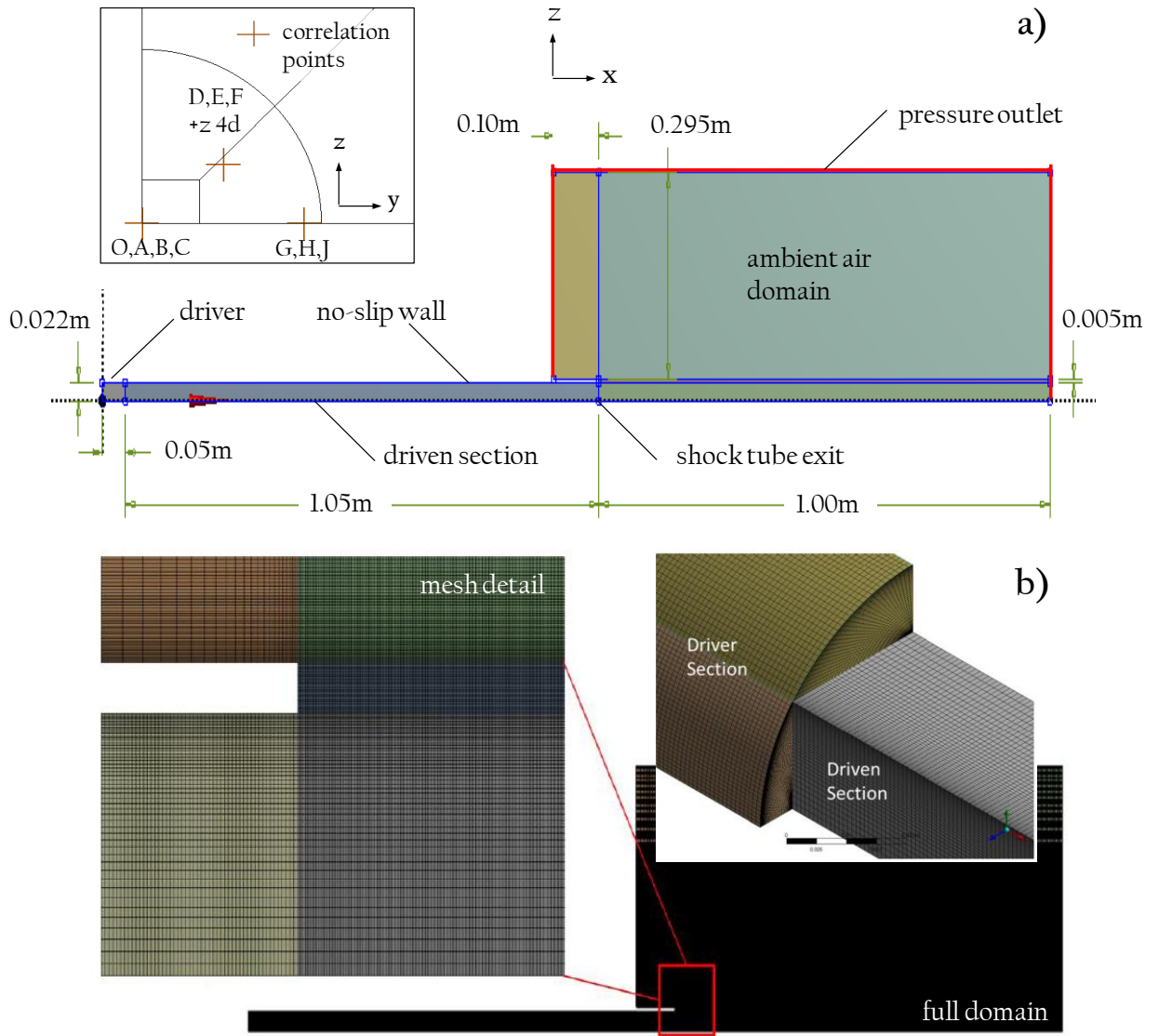
Fig. 5. CFD domain and boundary representations (a) for reproducing the small-scale tests, and (b) details of the mesh construction on the symmetry plane and in 3d.
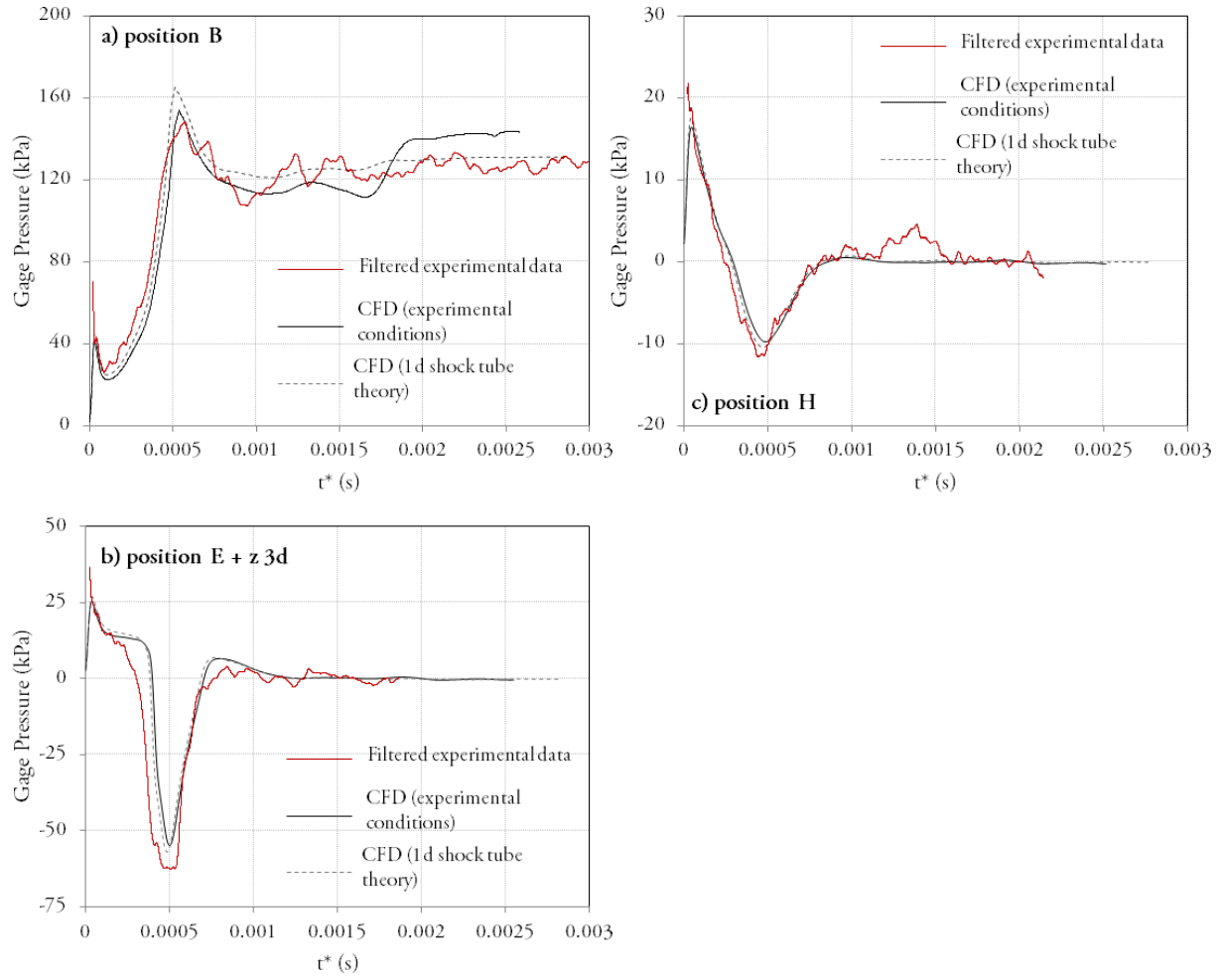
Fig. 6 CFD predictions of gage pressure at three sample positions vs. t*, for both inlet boundary conditions as compared to low-pass filtered experimental data.
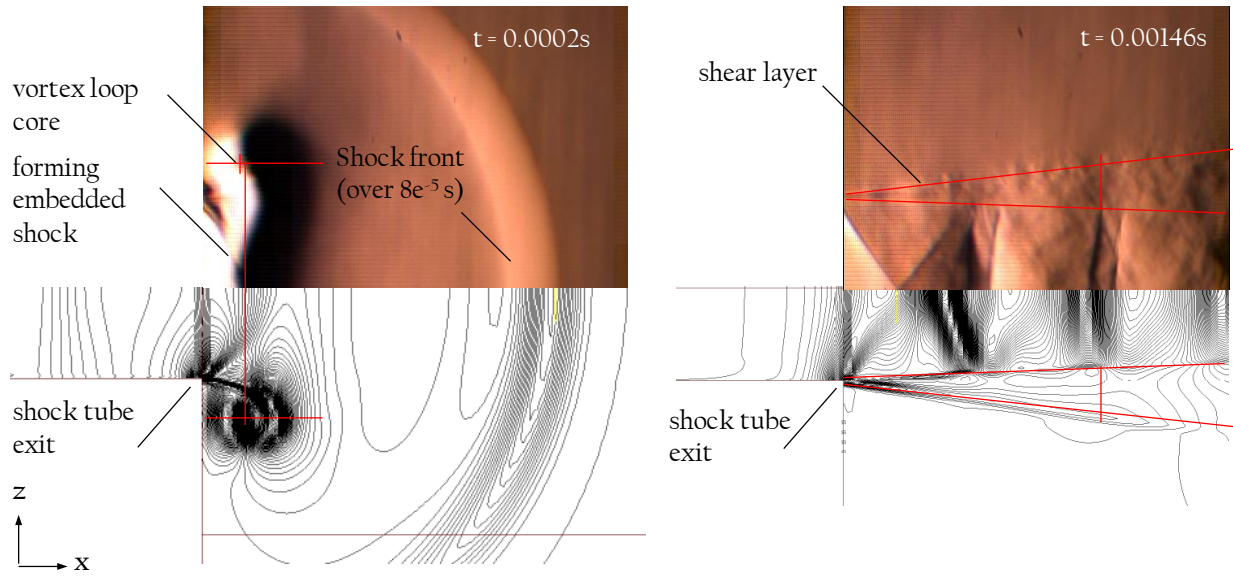
Fig. 7 CFD contours of density as compared to experimental Schlieren for free-exhausting (no flame) shock tube flow for 414 kPa driver stagnation pressure, using k-ω SST turbulence model.
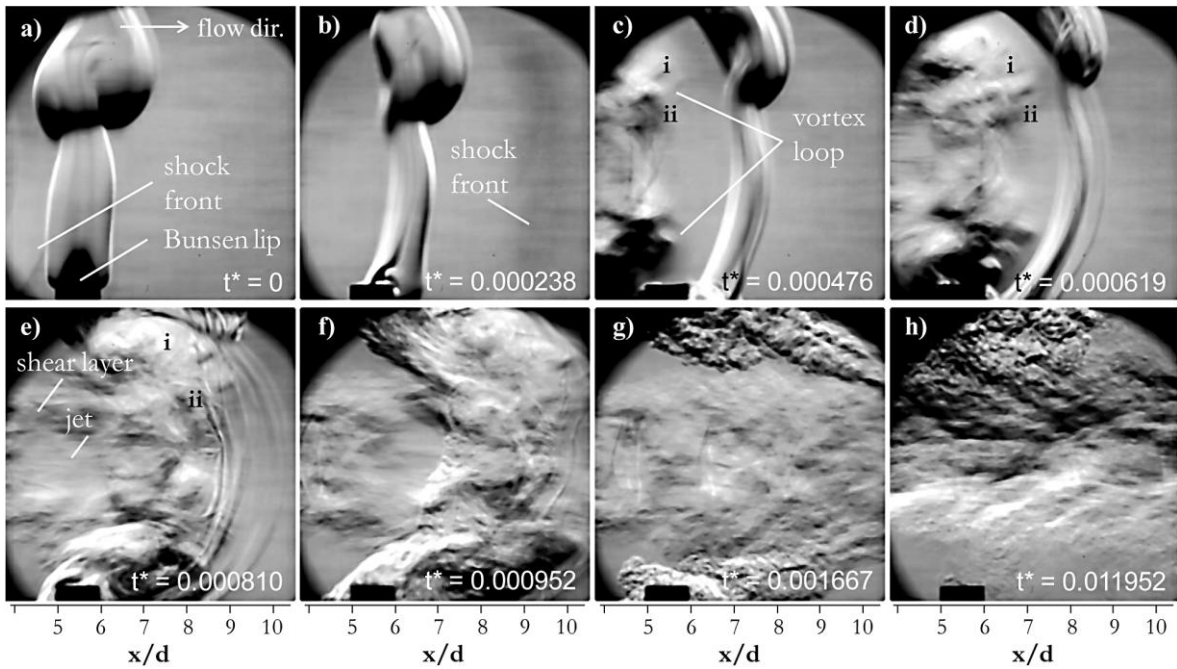
Fig. 8 Interaction type I, with flame at position A (x = 4.5 d, y = 0 d), for initial driver pressure of 414 kPa.
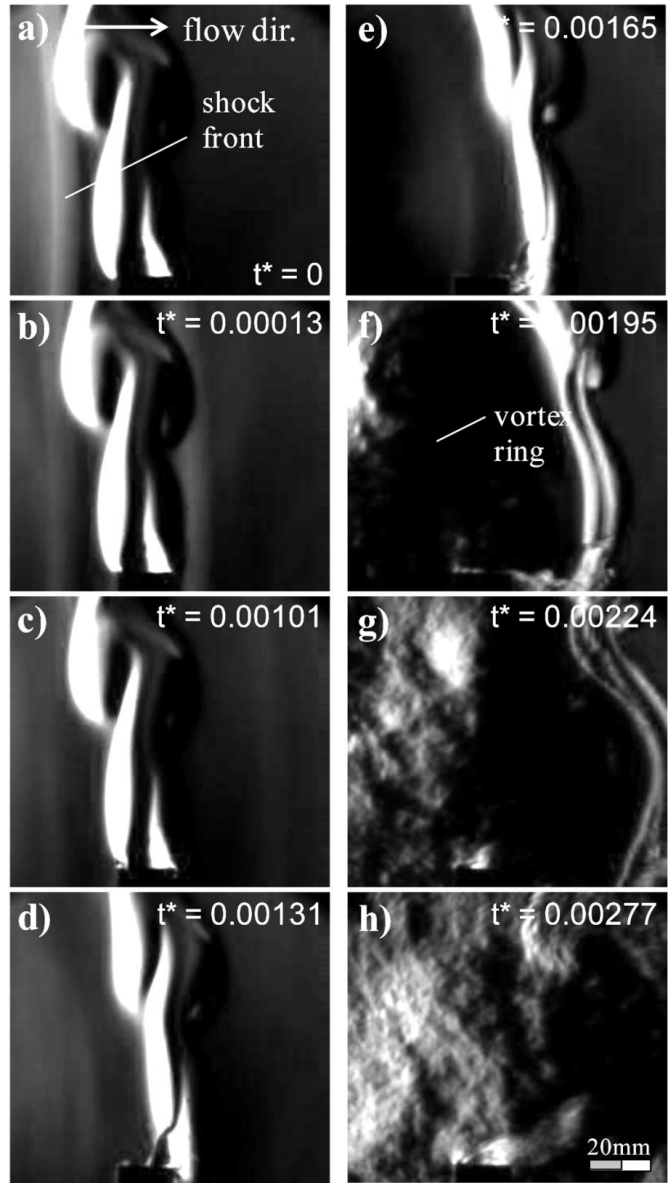
Fig. 9 Interaction type II, with flame at x = 25 d, y = 0 d, for initial driver pressure of 414 kPa.
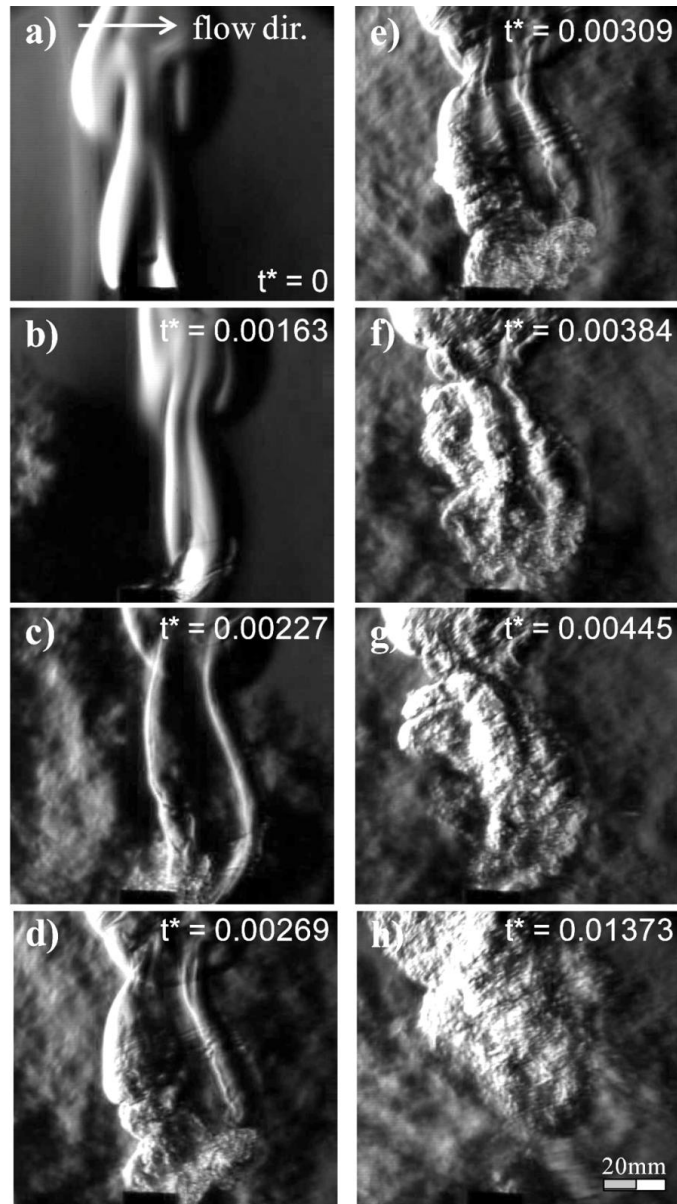
Fig. 10   Interaction type III, with flame at x = 7 d, y = 5 d, for initial driver pressure of 414 kPa.
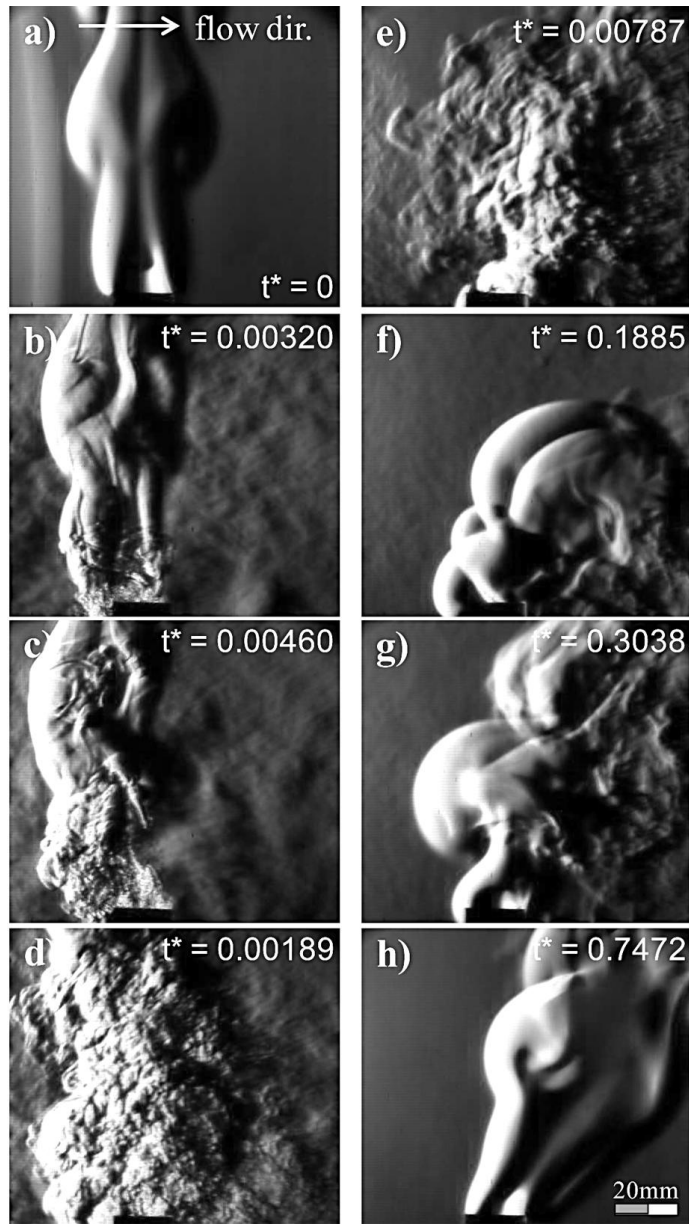
Fig. 11   **Interaction type IV, with flame at x = 25d, y = 12d, for initial driver pressure of 414kPa**
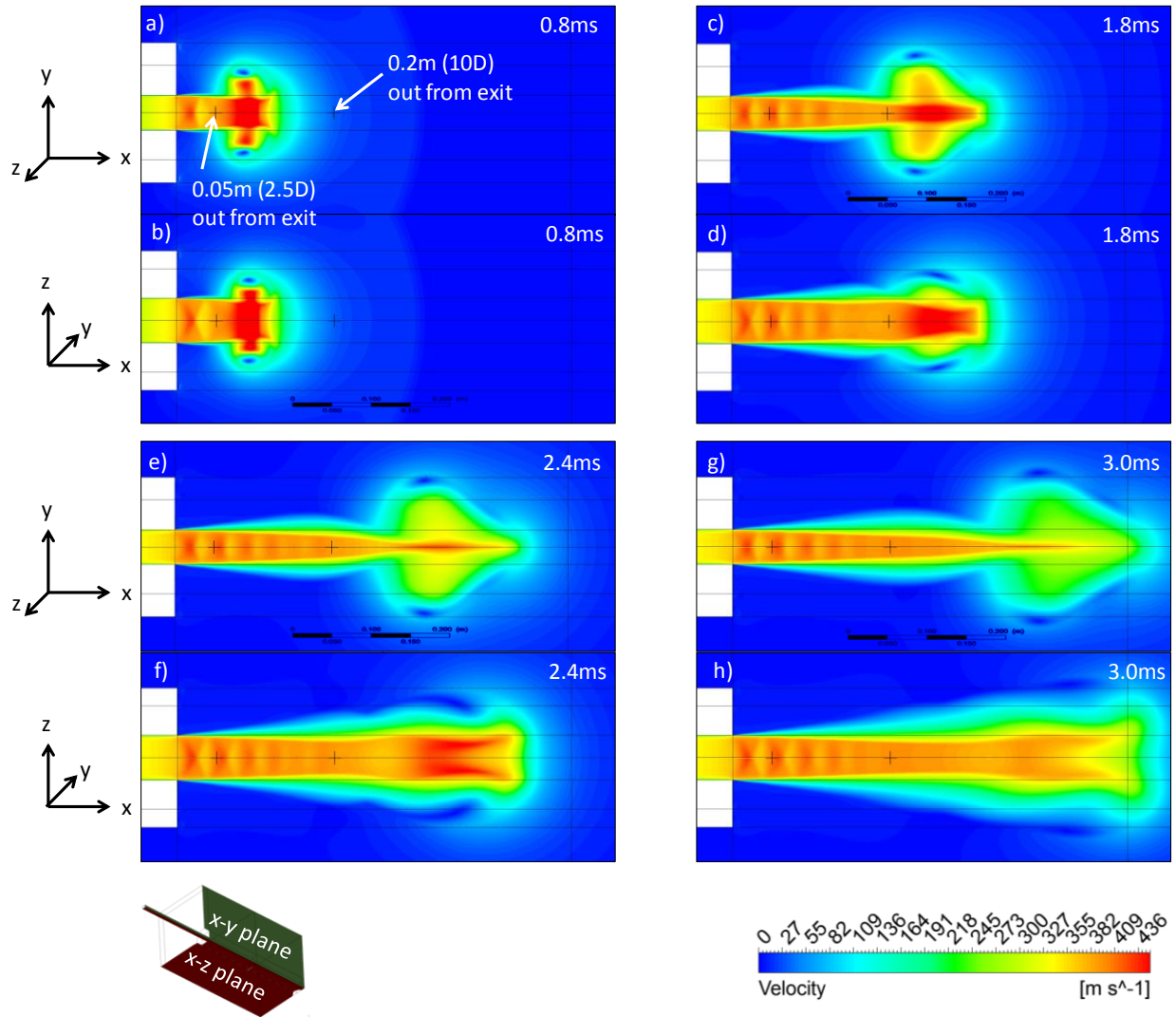
Fig. 12. CFD contour plot of velocity for flow exiting the shock tube as viewed side-on and top-down, at 4 different moments in time.
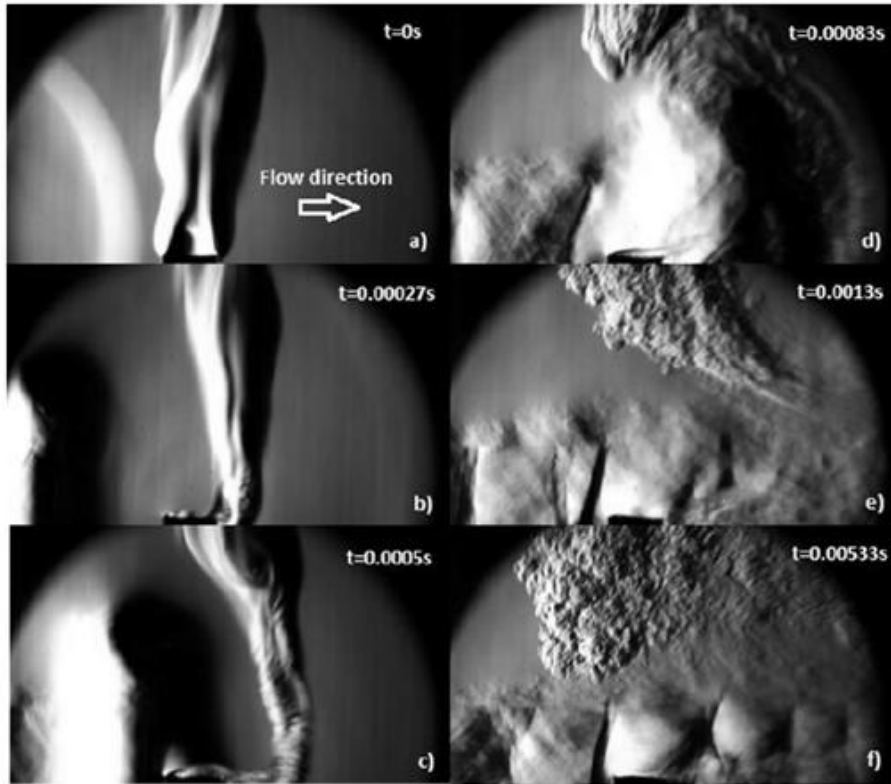
Fig. 13 Schlieren of shock/flame interaction at Bunsen flame location 4.5D (position A) on axis.
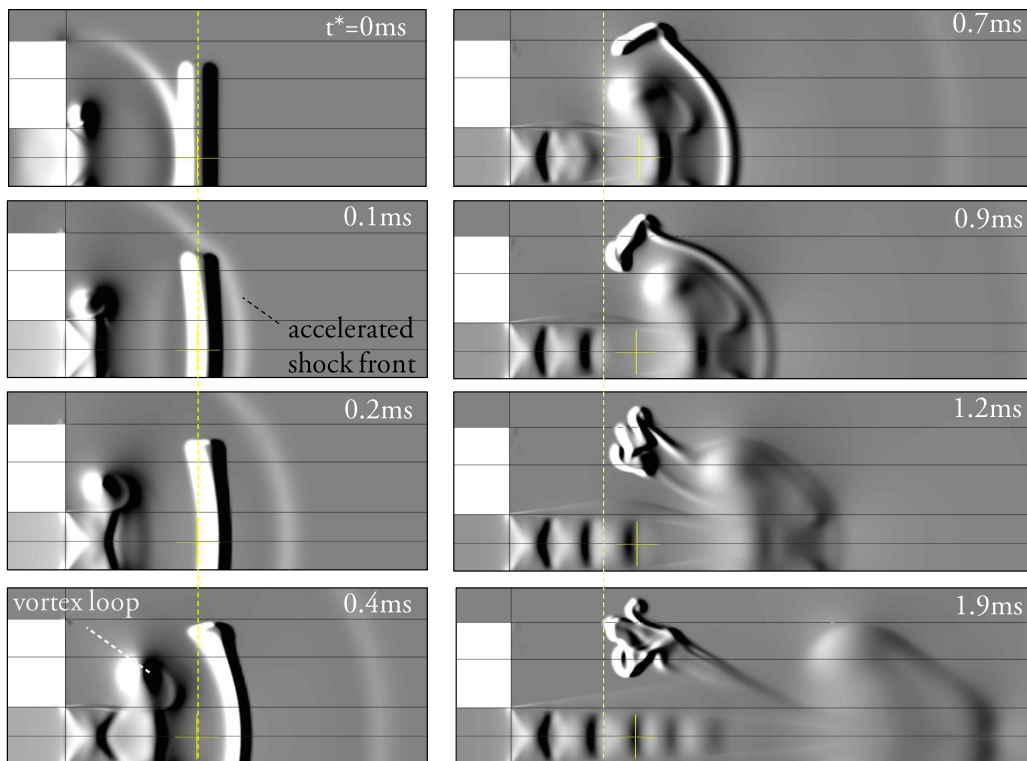
Fig. 14 Numerical schlieren of shock/heat interaction at Bunsen flame location 4.5D (position A) on axis.
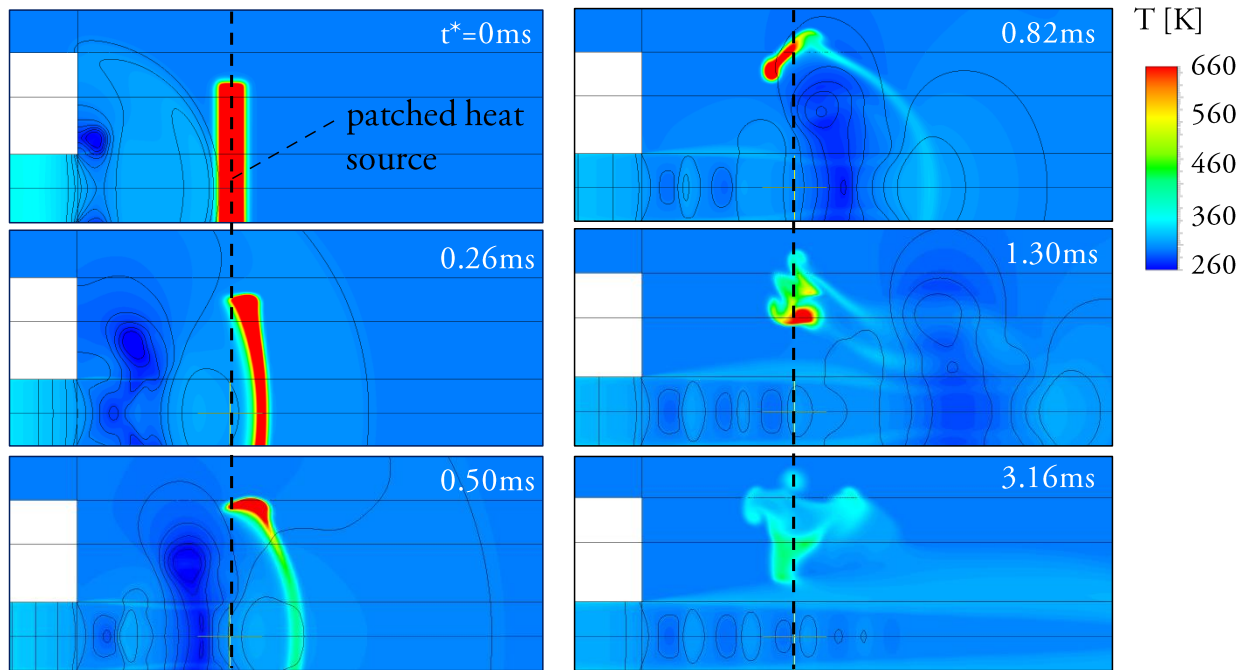
Fig. 15 CFD contours of temperature with time for shock/heat interaction at Bunsen flame location 4.5D (position A) on axis.
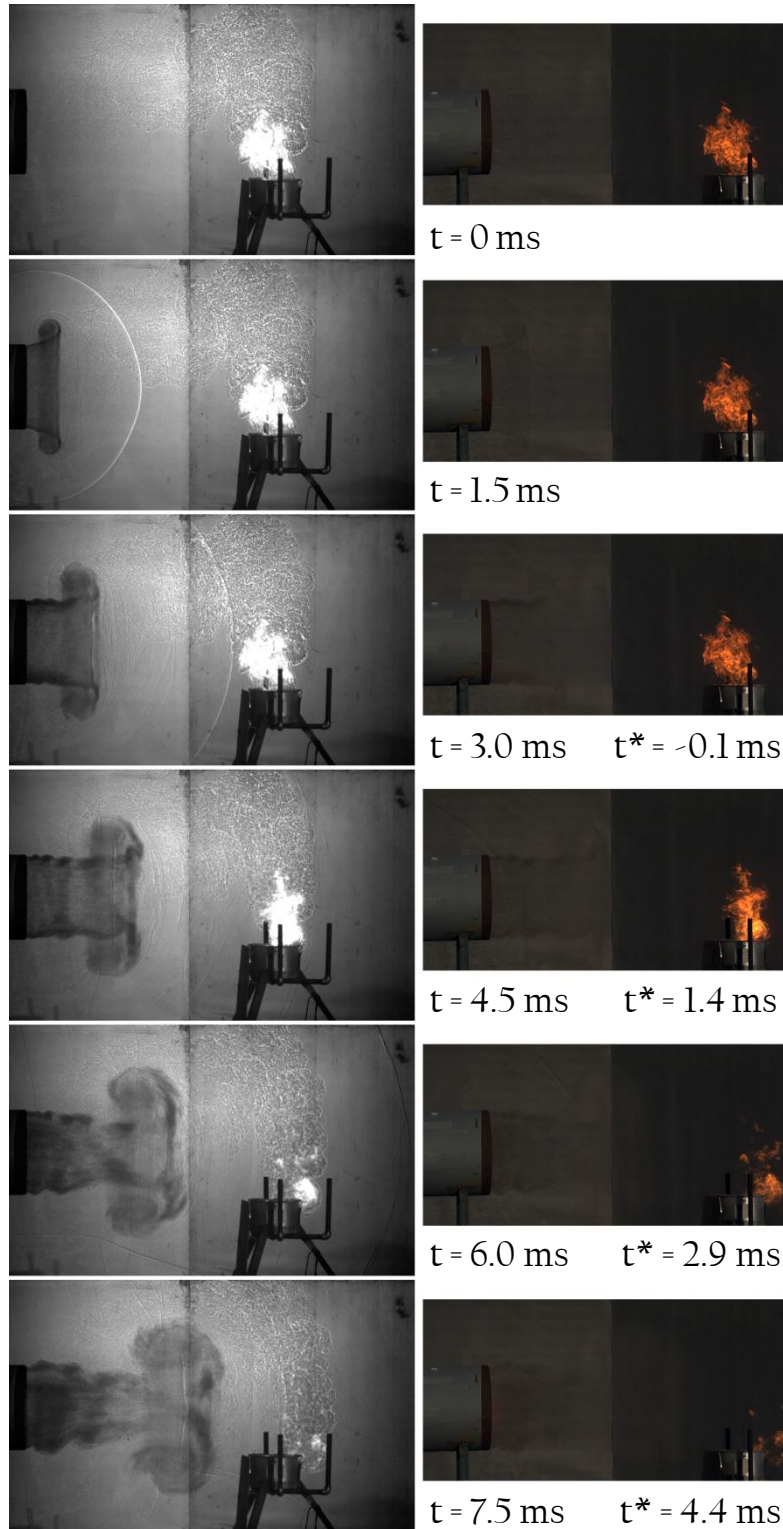
Fig. 16 Shadowgraph image sequence for position 4, large-scale tests at EMRTC, showing behavior and timescale of extinguishment of flame (fully extinguished at t* = 6.5ms, not shown here).
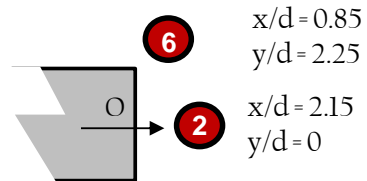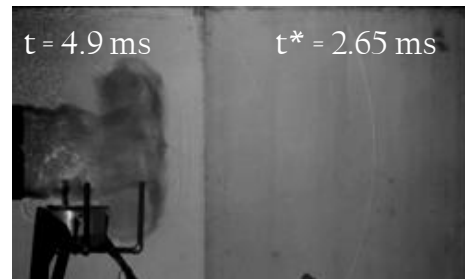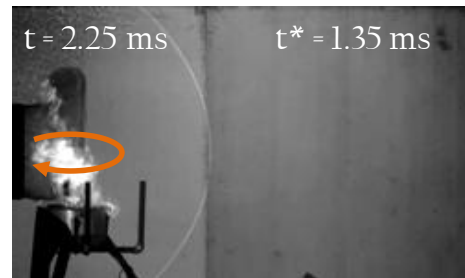
Position 2

t = 0 ms

t = 1.5 ms   t* = 0 ms

t = 2.4 ms   t* = 0.9 ms

t = 4.35 ms   t* = 2.85 ms

t = 11.35 ms   t* = 9.85 ms

Position 6

t = 0 ms

t = 0.9 ms   t* = 0 ms

t = 2.25 ms   t* = 1.35 ms

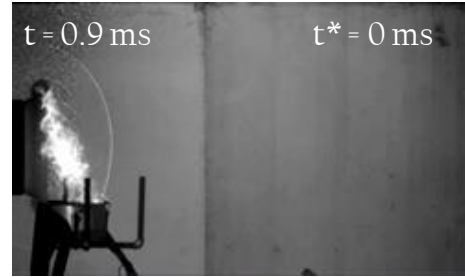t = 4.9 ms   t* = 2.65 ms

x/d = 0.85
y/d = 2.25

x/d = 2.15
y/d = 0
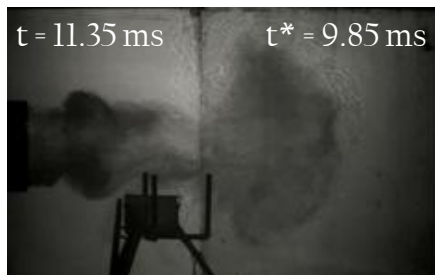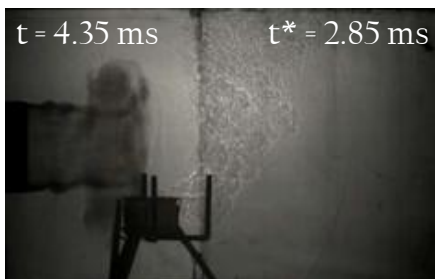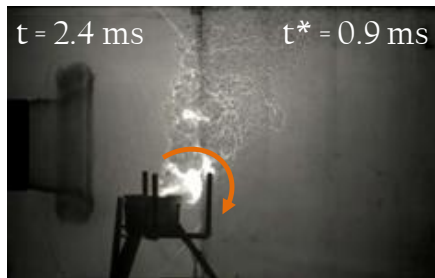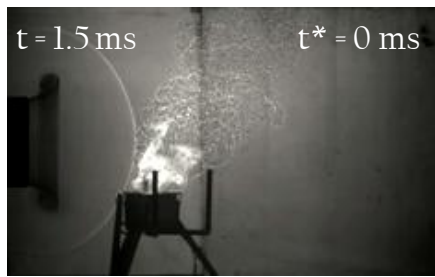
Fig. 17 Shadowgraph image sequence for positions 2 and 6 (large-scale tests at EMRTC) showing behavior and timescale of extinguishment of flame.
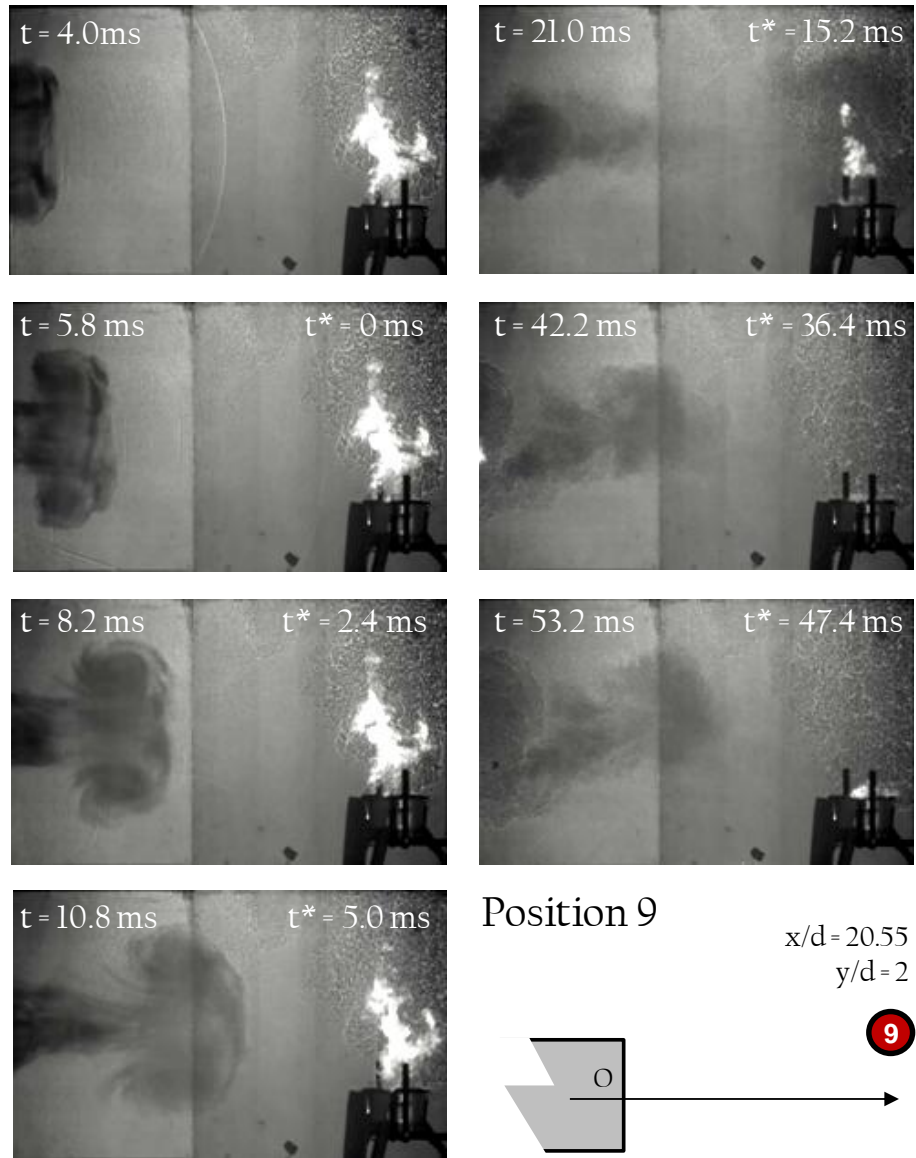
Fig. 18 Shadowgraph image sequence for position 9 (large-scale tests at EMRTC) showing behavior and timescale of extinguishment of flame, with subsequent re-ignition at t* = 47.4ms.